Available online at www.sciencedirect.com

ScienceDirect

Advances in Space Research 52 (2013) 1366–1377

Advances in Space Research (a COSPAR publication)

www.elsevier.com/locate/asr

Tunable filters for multispectral imaging of aeronomical features

C. Goenka [a,*], J.L. Semeter [a], J. Noto [b], H. Dahlgren [a], R. Marshall [c], J. Baumgardner [a], J. Riccobono [b], M. Migliozzi [b]

[a] Boston University, 8 St Mary's Street, Boston, MA 02215, USA
[b] Scientific Solutions Inc (SSI), 55 Middlesex Street, Unit 210, North Chelmsford, MA 01863, USA
[c] Stanford University, 350 Serra Mall, Stanford, CA 94305, USA

Received 30 November 2012; received in revised form 4 June 2013; accepted 7 June 2013
Available online 29 June 2013

Abstract

Multispectral imaging of optical emissions in the Earth's upper atmosphere unravels vital information about dynamic phenomena in the Earth-space environment. Wavelength tunable filters allow us to accomplish this without using filter wheels or multiple imaging set-ups, but with identifiable caveats and trade-offs. We evaluate one such filter, a liquid crystal Fabry–Perot etalon, as a potential candidate for the next generation of imagers for aeronomy. The tunability of such a filter can be exploited in imaging features such as the 6300–6364 Å oxygen emission doublet, or studying the rotational temperature of N_2^+ in the 4200–4300 Å range, observations which typically require multiple instruments. We further discuss the use of this filter in an optical instrument, called the Liquid Crystal Hyperspectral Imager (LiCHI), which will be developed to make simultaneous measurements in various wavelength ranges.
© 2013 COSPAR. Published by Elsevier Ltd. All rights reserved.

Keywords: Fabry–Perot; Liquid crystal; Multispectral; Rotational temperature; Tunable filter; Aeronomy

1. Introduction

Optical emissions in the Earth's upper atmosphere serve as an important source of information regarding the physical processes underlying the upper atmosphere and its connection with the space environment. These emissions have long been observed using a myriad of ground-based techniques including monochromatic imaging systems (e.g. Baumgardner et al., 1992), networks of monochromatic imaging systems such as ALIS (Steen, 1989; Gustavsson, 2000; Carl-Fredrik Enell, 2002; Brändström, 2003) and MIRACLE (Syrjäsuo et al., 1998; Amm et al., 2000), simultaneous multispectral imagers such as the SMI (Semeter et al., 2001) and ASK (Dahlgren et al. 2008a; Lanchester et al., 2009) and spectrographs such as HiRISE (Pallamraju et al., 2001) and HiTIES (Chakrabarti et al., 2001). More recently, electro-optical tunable filters have found increased use in ground-based aeronomical imaging instruments because of their ability to obtain spatial information as well as spectral information over a large wavelength range. Examples of these instruments include an automated spectrometer used by Shiokawa et al. (2002) which uses acousto-optical tunable filters (AOTF) to observe the OI 5577 Å line, NORUSCA cameras (Sigernes et al., 2012) which use liquid crystal tunable filters (LCTF) for hyperspectral imaging of aurora and airglow, etc. This article discusses the possibility of using a tunable Liquid Crystal Fabry–Perot (LCFP) etalon for multispectral imaging in aeronomical studies.

Fabry–Perot etalons have traditionally been used as high resolution interferometers by aeronomers for line profiling and Doppler shift measurements in various configurations, including wavelength scanned etalons, depending on the application. A standard Fabry–Perot interferometer

* Corresponding author. Tel.: +1 857 207 9440; fax: +1 617 353 7337.
E-mail addresses: cgoenka@bu.edu (C. Goenka), jls@bu.edu (J.L. Semeter), noto@sci-sol.com (J. Noto), hannad@bu.edu (H. Dahlgren), ram80unit@gmail.com (R. Marshall), jeffreyb@bu.edu (J. Baumgardner), nita@sci-sol.com (J. Riccobono), mike@sci-sol.com (M. Migliozzi).

0273-1177/$36.00 © 2013 COSPAR. Published by Elsevier Ltd. All rights reserved.
http://dx.doi.org/10.1016/j.asr.2013.06.014

(FPI), with fixed plate spacing, was used by Sivjee et al. (1980) with a TV imaging system for real-time observations of weak auroral 5577 Å and 6300 Å emissions. A spatial scanning, imaging Fabry–Perot spectrometer with capacitive feedback stabilization was used by Bahsoun-Hamade et al. (1994) to measure the OI 8446 Å emission. A Fabry–Perot etalon can be scanned in wavelength by either changing the spacing between its plates, e.g. by using piezoelectric spacers (Hernandez and Mills, 1973; Rees et al. 1981), or by changing the refractive index of the material contained in the gap between the plates, e.g. pressure scanned etalons (Burnett and Burnett, 1983). Piezoelectrically scanned etalons have a higher finesse and range of operation than pressure scanned etalons (Chandrasekhar et al., 1988), making them a more popular choice among aeronomers. They have been used by Conde and Smith (1998) and, in a triple-etalon system, by Gerrard and Meriwether (2011) for observation of thermospheric winds by measurement of the OI 6300 Å emission. These instruments derive spatial and spectral information by imaging the rings formed by the etalon. Fabry–Perot etalon can alternatively be used as an interference filter, which works on the same principle as the FPI but has a smaller spacing between its plates and operates within its Jacquinot spot.

A Fabry–Perot interference filter, like the FPIs, can also be scanned in wavelength. However, piezoelectric methods are prone to mechanical errors due to movable plates and require very careful tuning due to the property of hysteresis demonstrated by piezoelectric crystals (Atherton, 1995). A liquid crystal filled Fabry–Perot interference filter where the refractive index within the gap is changed by applying a voltage, is a solid state device with no moving parts (Schneller et al., 1998; Daly et al., 2000) and offers a more elegant solution for wavelength scanning. Owing to larger tuning ranges than AOTFs and better spectral resolution than the LCTFs used in NORUSCA cameras, LCFP etalons are deemed better suited to our application. In the rest of the discussion, the term etalon will refer to a Fabry–Perot interference filter.

Despite their increased use, a quantitative assessment of electro-optical tunable filters specific to the field of aeronomy has not yet been reported in detail. This article analyzes the capabilities and limitations of LCFP etalons through simulation and presents a methodology for using them in specific application areas in aeronomical science. We also discuss the possibility of making simultaneous measurements of aeronomical features using only one optical chain and one detector by constructing a four-channel optical instrument, using four LCFP etalons, each with a different gap size, and individually tunable.

Section 2 provides a background for LCFP technology, Section 3 presents modeling results and calculations to illustrate the performance of this device for two classes of aeronomical investigations and Section 4 describes a specific instrument, the Liquid Crystal Hyperspectral Imager (LiCHI), based on a four-channel tunable LCFP etalon.

2. Technical background – Fabry–Perot liquid crystal filters

A Fabry–Perot etalon is made of two partially reflective plates, parallel to each other. Interference occurs due to multiple successive reflections of light between the two plates (Vaughan, 1989). The intensity transmitted through the etalon, as a function of wavelength, λ, and angle of incidence, θ, is given by the Airy function

$$I(\theta,\lambda) = (I_0)(\lambda)\frac{1}{1+\left(\frac{2F}{\pi}\right)^2\sin^2\left(\frac{\delta}{2}\right)} \tag{1a}$$

$$\delta = \frac{4\pi d\mu\cos(\theta)}{\lambda} \tag{1b}$$

where I_0 is the incident spectral irradiance, the separation between the plates is given by d, μ is the refractive index of the material in the gap and F is the finesse of the etalon. The resulting interference pattern is a series of alternating bright and dark fringes which decrease in radius with increase in wavelength. Fig. 1 shows a typical spectral response of a Fabry–Perot etalon. Fabry–Perot etalons are preferred for their high spectral resolution while preserving image quality and yielding maximum throughput for a given spectral resolution. The high spectral resolution is needed to resolve individual emission lines in the airglow and aurora spectra, and a high throughput would enable the instrument to make measurements in low light conditions. The spectral resolution and the free spectral range (FSR) of the etalon are determined by the width of the gap between the plates. FSR is the spacing between two successive maxima or minima.

A liquid crystal filled Fabry–Perot etalon is used so that a wavelength region can be scanned without any mechanically moving parts, making the instrument robust. Liquid crystals exhibit the property of birefringence (De Gennes and Prost 1993), and therefore are tunable in wavelength. The molecules of the liquid crystal are rearranged by applying an external trigger such as voltage (Fig. 2), which causes the extraordinary refractive index which is 1.65 for the liquid crystal to tend towards the ordinary refractive index of 1.58. This change in refractive index shifts the resonant wavelength that is transmitted through the etalon. The change in wavelength with voltage is quick, smooth and can be carried out in very fine steps. This gives us a complete scan of the spectral region of interest. Fig. 3a shows the LCFP function and the order sorting filter function. Fig. 3b shows an example of the tuning of the etalon. A single order of the etalon transmission function from Fig. 1 is captured by the order sorting filter. The etalon is first tuned to a wavelength λ_1 as illustrated by the solid transmission curve and then to wavelength λ_2, shown as a dashed curve, by changing the voltage applied.

An etalon behaves as a narrow band-pass filter when the separation between the plates is very small resulting in large separation between transmission peaks (i.e. large FSR) and a large central monochromatic ring or Jacquinot spot (Jones et al., 2002). In order to use the LCFP as a

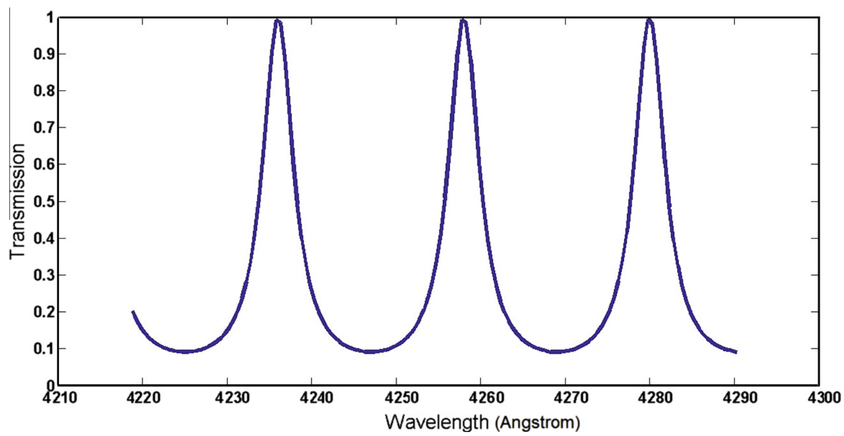

Fig. 1. Example of spectral response of a Fabry–Perot etalon showing transmission peaks for different orders of constructive interference, for a gap of 28 μm.

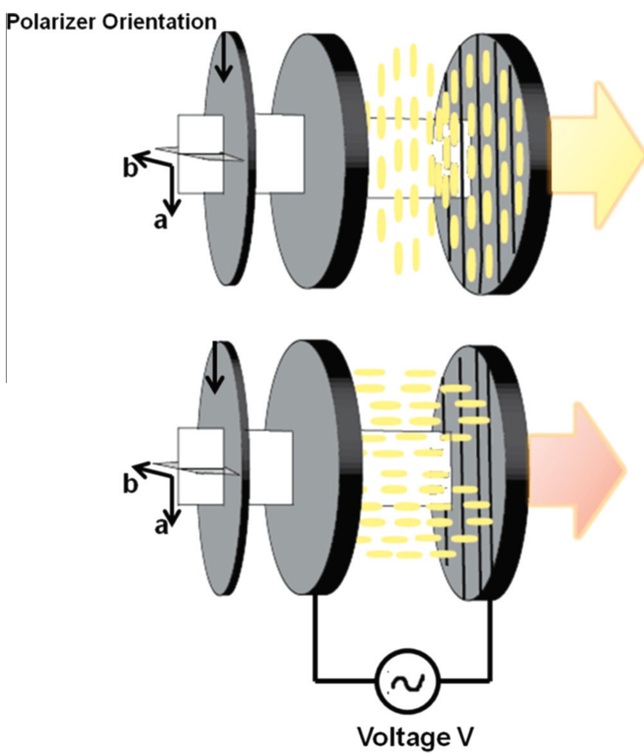

Fig. 2. Behavior of liquid crystal molecules in presence of voltage, with the top and bottom sketches showing the arrangement of molecules in the absence and presence of voltage, respectively. Only the light polarized in direction ‘a’ will be affected by the change in refractive index of the molecules and therefore light polarized in other directions is cut out by the polarizer.

tunable filter, two other components are needed in addition to the small gap. First, a polarizer is required to exploit the birefringence property of the liquid crystal, since only the light polarized parallel to the direction of the liquid crystal molecules is sensitive to the change in refractive index. Second, an order sorting filter is required to select and transmit only the desired order of interference. Both the polarizer and order-sorting filter have the negative effect of reducing the peak transmission. Although the resulting device is a low transmission, low resolution filter compared to the standard interference filters, the ability of the device to be tuned arbitrarily within its FSR provides a unique solution for specific aeronomical problems, as discussed in this report.

3. Application to scientific measurements

The transmission function of the LCFP in a certain wavelength region determines the feasibility of using it for scientific measurements in that region. For a given angle and an applied voltage, the output of a tunable filter can be represented as

$$Y(\lambda_t) = \int H(\lambda, \lambda_t) X(\lambda) d\lambda \tag{2}$$

where $Y(\lambda_t)$ represents the output intensity when the filter is tuned to central wavelength λ_t, $H(\lambda, \lambda_t)$ is the transmission of the LCFP at wavelength λ when the filter is tuned to λ_t, and $X(\lambda)$ is the input spectrum (Che et al., 2006). In this report, we use this transmission model of the LCFP, assuming normal incidence and refractive index between 1.58 and 1.63, to study its feasibility in two representative problems. For the first scientific investigation, the approach is to use one tunable filter to measure two emissions (the P and R branches of the N_2^+1NG (0,1) band) and use the ratio between them to derive the rotational temperature. We will also discuss how this informs the design methodology. In the second investigation we wish to extract narrow line features from a broad background (e.g. the 6300 Å forbidden line of atomic oxygen).

For our model, a discrete version of Eq. (2), $y = Hx$, is used where

$$H = \begin{bmatrix} h(\lambda_i, \lambda_{t1}) & \dots & h(\lambda_n, \lambda_{t1}) \\ \vdots & \ddots & \vdots \\ h(\lambda_i, \lambda_{tm}) & \dots & h(\lambda_n, \lambda_{tm}) \end{bmatrix} \tag{3}$$

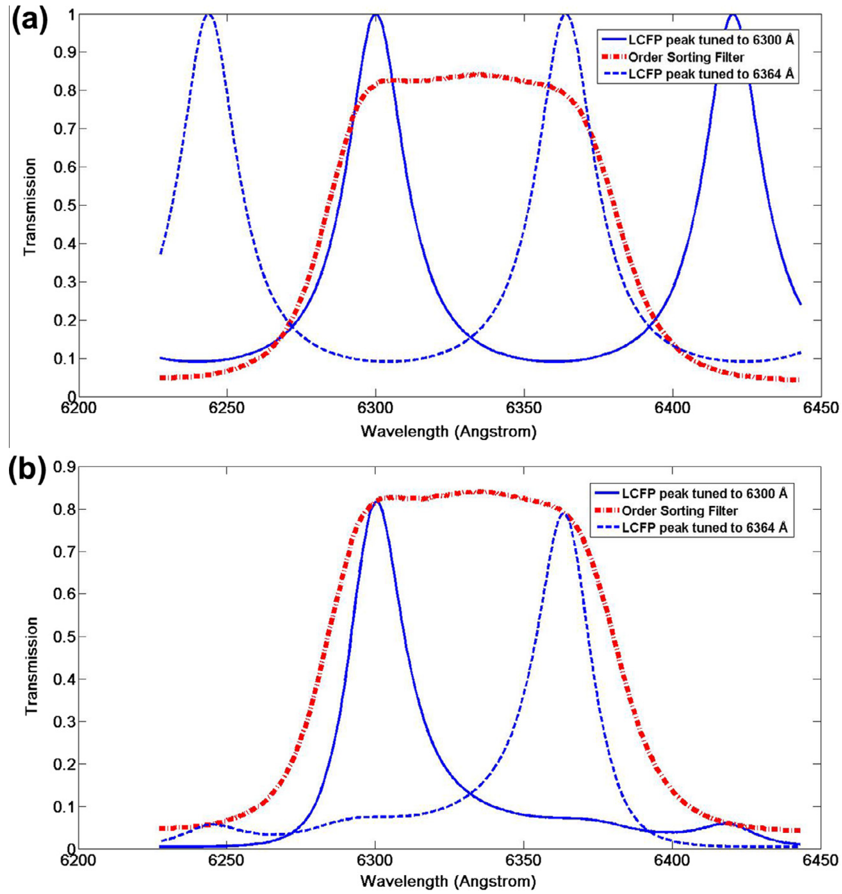

Fig. 3. (a) Transmission peaks of the LCFP for a gap of 10 μm tuned to 6300 Å and 6364 Å, and the transmission of the order sorting filter. (b) LCFP transmission function truncated by the order sorting filter transmission function.

with m being the number of central wavelengths to which the filter is tuned, and n being the wavelengths at which the filter characteristic is calculated.

The signal to noise ratio (SNR) performance of the system is evaluated by using the Eqs. (4a)–(4c) for an Andor Neo sCMOS 2160 × 2560 pixel detector.

$$SNR = \frac{n}{\sqrt{n + (d * t) + r^2}} \tag{4a}$$

where n is the number of photo electrons in a pixel, d is the dark current, t is the integration time and r is the read noise.

The number of photo electrons in a pixel can be approximated by

$$n = P * T * QE * t \tag{4b}$$

where P is the photon flux [photons/s] at the image plane for each pixel, T is the total transmission of the optical components in the system and QE is the quantum efficiency.

As 1 Rayleigh = $(1/4\pi)$ * 10^{10} photons s^{-1} m^{-2} sr^{-1} (Baker and Romick, 1976), the flux at a pixel is approximated by

$$P = B * \frac{10^{10}}{4 * \pi} * G \tag{4c}$$

where B [R] is the column emission rate and G [m^2 sr] is the etendue of the system for input optic with f/2.8, focal length of 2.5 cm and field of view of 40°.

The above equations are used for obtaining SNR estimates for the cases discussed later in the paper. The values of quantum efficiency, dark current and read noise were obtained from the technical specifications of the Andor Neo sCMOS detector, for which QE is a function of wavelength and varies between ∼0.4 and ∼0.6 in the wavelength range 4000–7000 Å, and d and r are assumed to be 0.015 e^-/s and 1 e^-, respectively. The transmission of the system is calculated by using transmission values of 70% for the LCFP, 50% for the polarizer, 80% for the order sorting filter and assuming all other optical components to be lossless.

3.1. N_2^+ *rotational temperature*

Measurements of neutral temperatures can be used to calculate the energies of the precipitating particles causing the auroral emissions. If the emitting species is in equilibrium with its local environment and the rotational temperature is in equilibrium with translational temperatures, the rotational temperature can be used as a measurement of neutral temperatures and the optical emission height can be derived, from which the energy of the precipitating electrons can be estimated. The altitude of the emissions determines the distribution of total band spectral column emission rate in various branches of a spectral band. The ratio of the spectral column emission rates of the P and R branches can reveal whether the changes in rotational temperature are due to heating or due to change in the height of the emissions (Romick et al., 1978). Rotational temperature measurements have been attempted using photometers, spectrometers, and spectral imaging systems, (see e.g. Jokiaho et al. 2008). Here we discuss the feasibility of using a LCFP filter for these measurements.

The wavelength band we have chosen for this feasibility study is the N_2^+1NG (0,1) band with a bandhead at 4278 Å. The P and R branches are centered around 4278 Å and 4258 Å, respectively. To measure the rotational temperature, the transmission peak of the etalon is first set to 4258 Å for the R branch and then tuned to 4278 Å to measure the spectral column emission rate of the P branch. The ratio is then calculated as

$$R(T) = \frac{y_P}{y_R} = \frac{\int_\lambda I(\lambda, T) H_P(\lambda) d\lambda}{\int_\lambda I(\lambda, T) H_R(\lambda) d\lambda} \tag{5}$$

where H_p and H_R represent the filter transmission function for each of the P and R branches. The filter transmission function H is basically the LCFP transmission function truncated by the transmission function of the order sorting filter.

The feasibility of using a LCFP etalon for this experiment depends on the gap between the plates of the etalon. The gap needs to be chosen carefully using the following criteria:

(a) The ratio R, in Eq. (5), should always be greater than 1. A value of R less than 1 indicates overlapping of interference orders, or an FWHM too broad to separate the P and R branches from each other. Since the gap determines the FWHM of the etalon, this criterion is critical in selecting the gap size.
(b) The selected gap should allow the instrument to measure the maximum range of rotational temperatures possible.
(c) There should be significant and detectable change in R with change in rotational temperature. The gap which results in most significant change in R with rotational temperature will be selected as the optimal gap.
(d) Ideally for an application like this, the instrument should be able to detect the smallest changes in rotational temperature. The selection of the gap will depend on the minimum change that can be detected by the instrument.

In this analysis, the N_2^+1NG spectra were generated for various rotational temperatures using the software Specair (Laux 2002) to the levels of medium intensity aurora ($\sim$20 kR) and are shown in Fig. 4. These spectra were sampled using the detector and optics described in Eq. (4) for an integration time of 1 s to get an SNR > 3, convolved with the LCFP instrument function for this analysis, and form the X in Eq. (2). For this application, the filter needs to be tuned to make measurements at only two central wavelengths, λ_{t1} and λ_{t2}, which are 4258 Å and 4278 Å, respectively. H, from Eq. (3), is then written as

$$H = \begin{bmatrix} h(\lambda_i, \lambda_{t1}) & \dots & h(\lambda_n, \lambda_{t1}) \\ h(\lambda_i, \lambda_{t2}) & \dots & h(\lambda_n, \lambda_{t2}) \end{bmatrix} \tag{6}$$

From this, y_P and y_R are calculated for P (4278 Å) and the R (4258 Å) branches, respectively, and their ratio is the ratio value R. This ratio changes with rotational temperature and etalon gap size as shown in Fig. 5(a). Fig. 5(b) shows the measured ratio in an ideal case where the filter response is an impulse function at the 4258 Å and 4278 Å wavelengths. From Fig. 5(a), one can infer that very small gaps, e.g. 1.2 μm, 4 μm, 6 μm, result in ratios which tend towards 1 and below 1 for high rotational temperatures, therefore not satisfying our first criterion on R (criterion (a) above). A similar behavior is shown by a large gap size of e.g. 25 μm. The gap sizes of e.g. 15 μm, 17.5 μm and 20 μm satisfy this first requirement over the same rotational temperature range as well as satisfying criterion (b). Criterion (c) and (d) help determine which gap to select out of the gaps satisfying criterion (a). As seen in Fig. 5(c), the maximum change in ratio, represented as the standard deviation in measured ratio, is seen for the 15 μm gap, which therefore becomes the desired gap for measurements of N_2^+ rotational temperatures. In our simulation, the source of error in the measured ratio is the uncertainty in the measurements made by the instrument, i.e. the noise in the measurements. Fig. 5(d) shows the measured ratio and the error in measured ratio for 15 μm gap LCFP, using the detector and optics described in Eqs. (4a)–(4c) with integration time of 1 s. This ratio ranges from 2.9 ± 0.2 to 1.2 ± 0.03. The smallest measureable change in rotational temperature is 75 K and increases with increase in rotational temperature. The error in ratio can be reduced by increasing integration times.

3.2. Background subtraction

The second application for which we want to test the feasibility of using a tunable filter is to extract line features from a broad background. In aeronomy, examples of such cases are the atomic oxygen line O(^{1}D–^{1}S) at 5577 Å embedded in a broad background, the atomic oxygen emission O(^{3}P–^{1}D) doublet at 6300 and 6364 Å, and the atomic oxygen emission O(^{2}D–^{2}P) multiplet at 7320–7330 Å. These representative cases are shown in Fig. 6. Tunability gives us the advantage of being able to measure the background using the same filter and the flexibility to study other emission lines in the vicinity of the main emission line, e.g. the 6364 Å oxygen line close to the 6300 Å line,

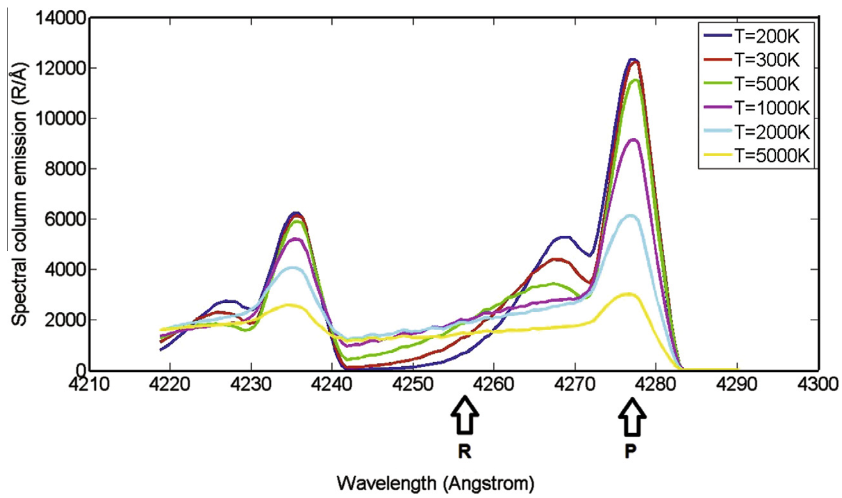

Fig. 4. N_2^+1NG spectra, showing changes in the spectral column emission rates at 4258 Å (*R* branch) and 4278 Å (*P* branch) with change in temperature. The spectra were generated using the Specair software (Laux, 2002).

or the hydroxyl lines in the vicinity of the 7320 Å multiplet. The spectrum around the emission of interest can then be computed from the measurements made with the filter.

3.2.1. 5577 Å and 6300 Å lines

For the measurement of the 5577 Å atomic oxygen line, the etalon peak will be tuned to a central wavelength, λ_t, of 5577 Å to measure the brightness of the line itself and then to another adjacent wavelength for the measurement of the background. A similar procedure can be followed for the measurement of the 6300 Å line, for which the etalon peak can be tuned to 6300 Å, 6364 Å and another wavelength within the etalon FSR to measure the background.

3.2.2. 7320 Å multiplet

The measurement of the atomic oxygen emission $O(^2D–^2P)$ multiplet at 7320–7330 Å poses a challenge as the etalon function width is larger than the individual lines of the multiplet. There are also OH and N_2 emission bands overlapping this spectral region (e.g. Dahlgren et al., 2008b), and careful spectral analysis will be needed to determine their contribution to the signal. In such a case, the spectrum can be computed from the measurement by using deconvolution techniques.

Here we explain the computation of the spectrum by setting up a numerical simulation for the 7320 Å emission. The spectrum along with the background are modeled using estimated numbers from Fig. 6(b). A maximum value of 100 R/Å is used in the modeled spectrum to get a total of 600 R for the emission at 7320 Å. To measure the 7320 Å emission line, the 7330 Å line and the background, the filter transmission function is scanned over the wavelength region of interest as shown in Fig. 7. The figure shows the modeled spectrum as a solid curve and the LCFP filter scan as dashed curve, truncated by an order-sorting filter. The transfer function is given by Eq. (3) as the filter is tuned to multiple central wavelengths and the measurement vector is constructed using a discrete version of the convolution function in Eq. (2). Two different techniques are used to deconvolve the spectrum measured by the LCFP, the Moore–Penrose pseudoinverse method (Prasad and Bapat 1992), which is a standard inversion technique, and the Nelder–Mead method (Nelder and Mead 1965), which is a nonlinear minimization technique. The Moore–Penrose method is a standard linear least squares minimization technique and computes the spectrum x_{MP} as $x_{MP} = y.H^{-1}$ where y is the LCFP measurement and $H^{-1}$is the pseudoinverse of the LCFP transmission function H. This deconvolved input spectrum can then be used to estimate y_{MP}, i.e. the measurement if the input spectrum was x_{MP}.

The Nelder–Mead method optimizes the agreement between the model and the measurements by minimizing their difference which we represent using a chi-square cost function. We use prior information about the spectrum, for example the spectral position of the emissions, ratio of different components of the spectrum, etc. to constrain the Nelder–Mead minimization. Using this information provided, Nelder–Mead minimization technique estimates the input spectrum x_{NM}.

The input spectra x_{MP} and x_{NM} are then used to estimate y_{MP} and y_{NM}, which are the respective outputs if the input spectra were x_{MP} and x_{NM}. The outputs y_{MP} and y_{NM} are calculated and shown in Fig. 8(a) along with the simulated LCFP measurements as the LCFP transmission function is scanned over the desired wavelength region. Fig. 8(b) shows the deconvolved input spectra x_{MP} and x_{NM} along with the original input spectrum. Despite the similarity between the estimated outputs in Fig. 8(a), the Nelder–Mead method outperforms the Moore–Penrose method in deconvolution of the input spectrum from the measured and estimated data. Nelder–Mead accurately deconvolves the spectrum and gives total column emission rate of each of the 7320 Å and 7330 Å emissions as measured by the LCFP and displays clearly the advantage of having prior information about the spectral emissions we want to measure.

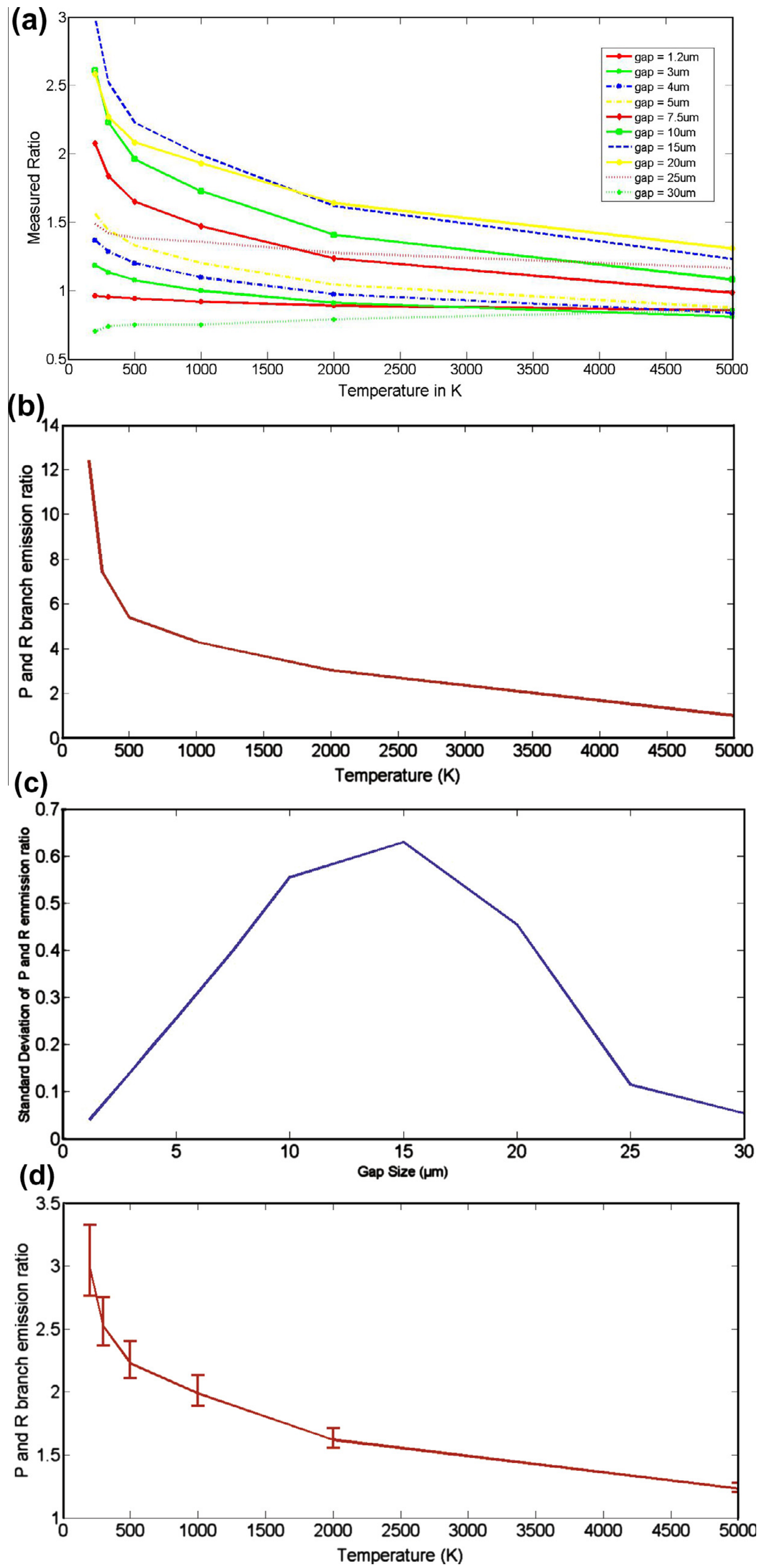

Fig. 5. (a) Change in P and R branch emission ratio R with change in temperature from 200 K to 5000 K for various gaps. (b) Ratio R for ideal case where the filter response is an impulse function at the wavelengths 4258 Å and 4278 Å. (c) Standard deviation of ratio, R, for different gaps, showing the maximum change in ratio with change in temperature obtainable for different gaps. (d) Measured ratio R for a gap of 15 µm.

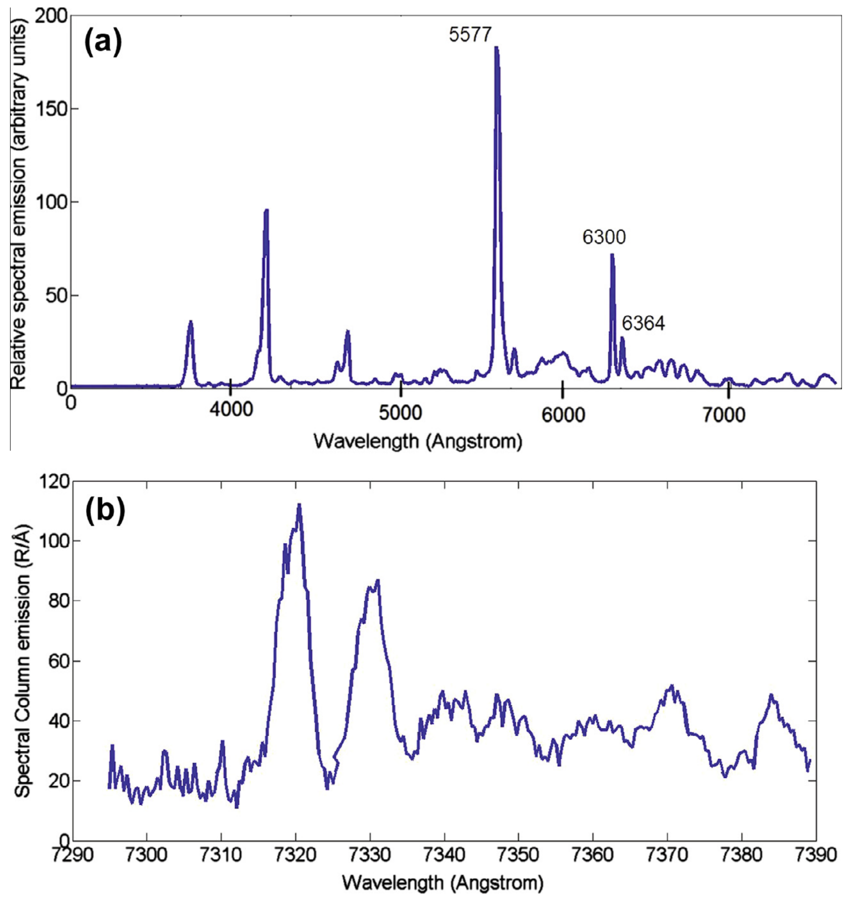

Fig. 6. Representative background subtraction cases – (a) the emission line at 5577 Å and the doublet at 6300–6364 Å embedded in a broad background (spectrum from Poker Flat, AK, courtesy of Jeff Baumgardner, CSP, Boston University). (b) The 7320–7330 Å multiplet (spectrum from HiTIES (Chakrabarti et al. 2001)).

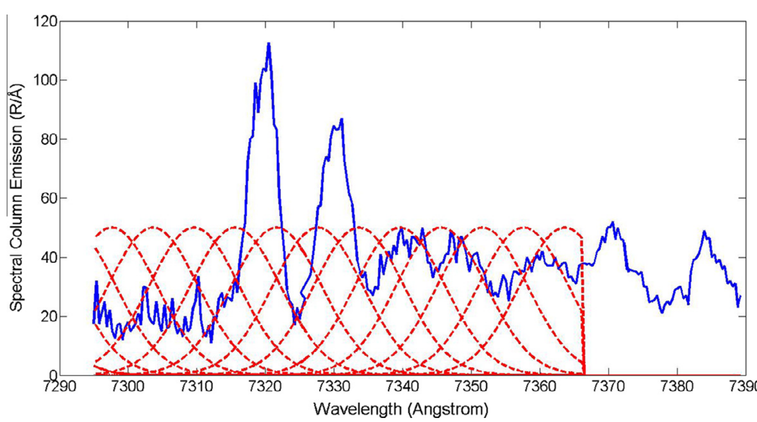

Fig. 7. A complete scan, shown as dashed curve, of the wavelength region of interest by the LCFP, making measurements of the background and of the two lines at 7320 Å and 7330 Å.

As for the constraints that the physical problem might post on the filter design, the model deconvolution algorithms described above can be tested with different gap sizes and the optimal gap can be chosen. A gap of 17.5 μm was chosen through this analysis for the 7320 Å multiplet measurement. An ideal detector was used for the purpose of numerical simulation. Using the detector described in Eqs. (4a)–(4c), these spectra will need to be sampled with integration times $\sim$5 min to obtain an SNR $>$ 2 throughout the spectrum.

4. Instrument implementation

A narrowband tunable filter is physically constrained to operate within a limited free spectral range. In an LCFP filter, the gap between the plates of the etalon determines the

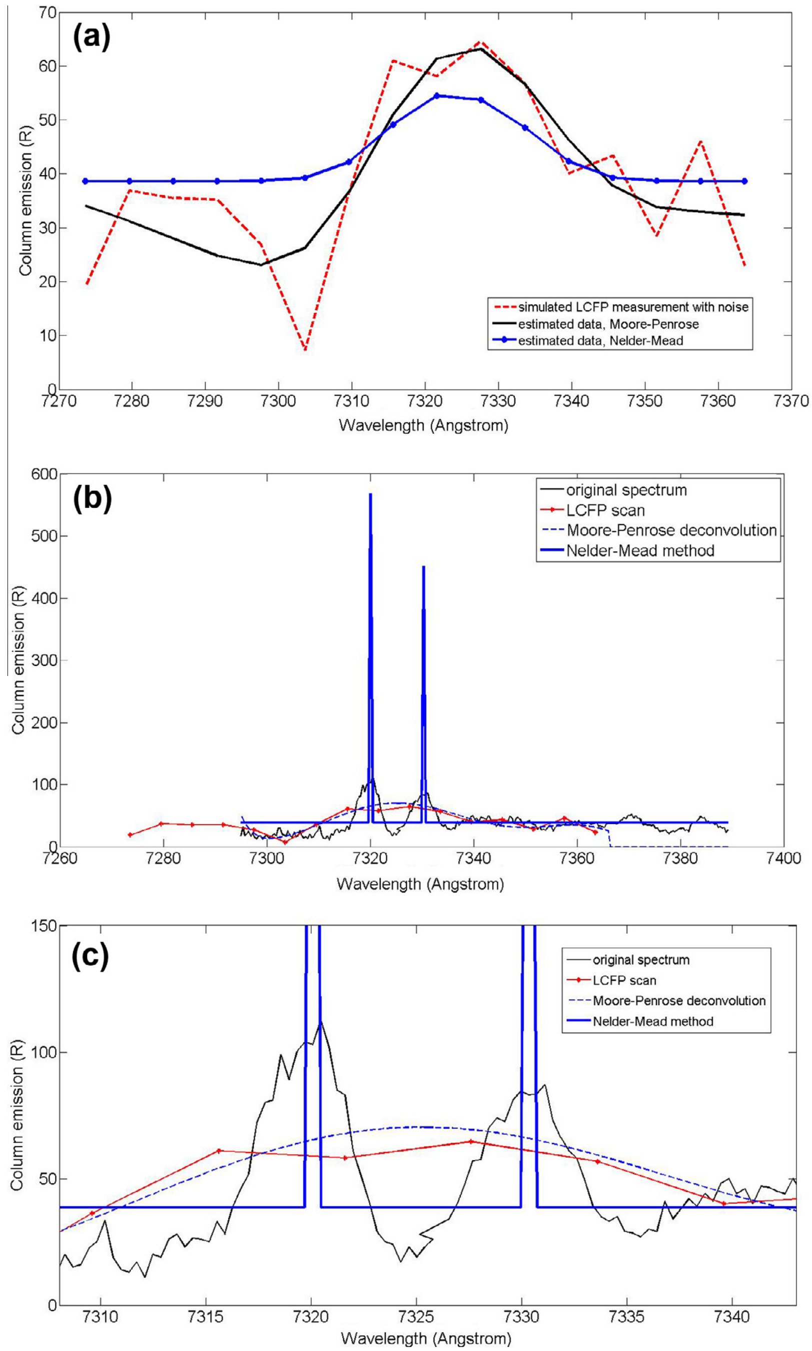

Fig. 8. (a) The simulated LCFP measurements, data estimated by two deconvolution methods (b) spectra deconvolved from the estimated data using two deconvolution methods (c) magnified version of Fig 8(b), showing the region with the 7320–7330 multiplet. As seen from this figure, a direct deconvolution of the measurements fails to resolve the column emission rates of the components of the multiplet, whereas the Nelder–Mead method which uses prior information about the location and known relative brightnesses of the peaks gives the column emission rates at the two peaks.

FWHM and FSR. The relationship between these two parameters is such that to obtain a large FSR, one must sacrifice spectral resolving power, and to have a high spectral resolving power, which is typically 10 or 20 Å for an aeronomical interference filter, one must sacrifice FSR, which means the instrument is designed for a particular wavelength region. While satisfying these requirements, the instrument also needs to have sufficient throughput such that we achieve a usable SNR for integration times that are shorter than the time scales for variability in the target we are studying.

Taking these requirements into account, we are developing an instrument using the LCFP filter technique. The instrument design is based on a previously developed instrument, called the Simultaneous Multispectral Imager (Semeter et al., 2001). Our new instrument is called the

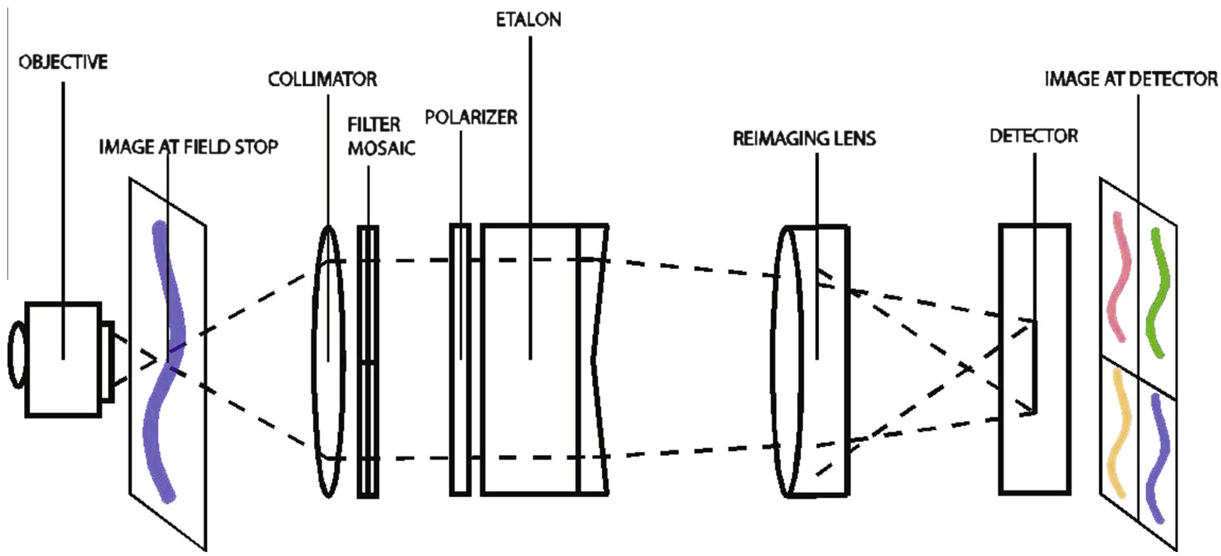

Fig. 9. The schematic of the Liquid Crystal Hyperspectral Imager (LiCHI), with the four-channel liquid crystal Fabry–Perot etalon at its heart along with the order sorting filter mosaic and the polarizer. The other components are objective lens, collimator to limit the angles into the etalon, reimaging lens and the detector (not to scale).

Liquid Crystal Hyperspectral Imager (LiCHI); the schematic of the instrument is shown in Fig. 9 (not to scale). It will use a four channel LCFP etalon with each channel designed for a different wavelength and focused to a different location on the detector through the use of wedge prisms. This system will be capable of measuring a limited number of wavelengths simultaneously, with the ability to tune each individual channel within its FSR.

Along with a four channel Fabry–Perot etalon, LiCHI will consist of front end optics, a collimator, an order sorting filter mosaic, a polarizer, a reimaging lens and a detector. The front end optics will include a combination of lenses designed to obtain a field of view of 40°. The collimator will limit the angles of the rays into the etalon. The angle into the etalon could range from 0 to 2.5 degrees, resulting in a wavelength shift of 4 Å. This would lie within the passband of the LCFP. The four channel LCFP etalon will have a prism array built into its structure in order to focus the light from different wavelength bands onto different regions in the detector, in combination with the reimaging lens.

A few improvements to the instrument can be envisioned to increase its functionality and control. LiCHI loses 50% of the light due to the polarizer, but the design can be enhanced to incorporate techniques to utilize the light with the undesired polarization (Zhang, 2008). Implementing an active temperature feedback loop will provide additional control to increase the precision of the measurements since liquid crystals are sensitive to temperature (Patel and Wullert 1992).

Similar instruments using a four channel etalon can be designed and developed for simultaneous multispectral imaging to address a broad range of problems not only in aeronomy but other areas of scientific research as well, while minimizing the complexity of the design. In aeronomy, the emissions discussed earlier in this paper can be measured using a four channel filter, with the channels tuned to 4278 Å, 6300 Å, 5577 Å and 7320 Å with appropriately chosen bandwidths. For industrial applications, four wavelength bands are proved to be enough to detect specific types of foreign materials in cotton (Jia and Ding, 2005), separating peeled shrimps from shells (Sigernes et al., 2000), and for other similar problems. In medical sciences, structures within the breast tissue can be distinguished from lesions based on their absorption and scattering properties at four wavelengths (Pifferi et al., 2003).

LiCHI is currently in development phase, and is expected to be completely built by fall of 2013. We plan to test it using controlled airglow signals produced artificially at the HAARP heating facility.

5. Summary and conclusion

We have presented a feasibility study for using tunable LCFP etalons to study common aeronomical emissions and discussed their capabilities and limitations. We have also discussed their use in constructing a novel multispectral imaging instrument. We have presented a framework for developing tunable filters for use in aeronomy. The optimal design specifications for the filters were investigated for comparing spectral column emission rates of P and R branches of N_2^+ emission to calculate rotational temperatures as well as for measuring emission lines and their surrounding spectral features. The model results presented in this paper show that LCFP etalons can be used for measurements of aeronomical features and a multispectral imager can be successfully designed to simultaneously measure four spectral regions, with each channel individually tunable in wavelength. The versatility of this imaging technique makes LCFP etalons useful for various other applications outside the field of aeronomy.

Tunable filters such as an LCFP etalon have unique capabilities and limitations. Although standard interference filters perform better in terms of spectral resolving power and transmitted intensity, the flexibility of LCFP tunable filters is useful in building a compact and versatile instrument.

Acknowledgement

This work was supported by the National Science Foundation under grant AGS 0960078.

Appendix A. Supplementary data

Supplementary data associated with this article can be found, in the online version, at http://dx.doi.org/10.1016/j.asr.2013.06.014.

References

Amm, O., Janhunen, P., Opgenoorth, H.J., Pulkkinen, T.I., Viljanen, A. Ionospheric shear flow situations observed by the MIRACLE network, and the concept of Harang discontinuity, in: AGU Monograph on Magnetospheric Current Systems, vol. 118, pp. 227–236, 2000.

Atherton, P.D., The scanning Fabry–Perot spectrometer, 3D optical spectroscopic methods in astronomy, in: ASP Conference Series, vol. 71, 1995.

Bahsoun-Hamade, F., Wiens, R., Moise, A., Shepherd, G. Imaging Fabry–Perot spectrometer for twilight observations. Appl. Opt. 33, 1100–1107, 1994.

Baker, D.J., Romick, G.J. The Rayleigh interpretation of the unit in terms of column emission rate or apparent radiance expressed in SI units. Appl. Opt. 15 (8), 1976.

Baumgardner, J., Flynn, B., Mendillo, M. Monochromatic imaging instrumentation for applications in aeronomy of the earth and planets. Proc. SPIE 1745, 1992.

Brändström, U. The Auroral Large Imaging System – Design, Operation and Scientific Results, Kiruna, IRF Scientific Report 279. ISBN 91-7305-405-4, 2003.

Burnett, C.R., Burnett, E.B. OH pepsios. Appl. Opt. 22 (18), 1983.

Carl-Fredrik Enell, Optical studies of polar stratospheric clouds and related phenomena, Kiruna, IRF Scientific Report 278. ISBN 91-7305-307-4, 2002.

Chakrabarti, S., Pallamraju, D., Baumgardner, J., Vaillancourt, J. HiTIES: a high throughput imaging echelle spectrograph for ground-based visible airglow and auroral studies. J. Geophys. Res. 106, 30337–30348, 2001.

Chandrasekhar, T., Debiprasad, C., Desai, J.N., Ashok, N.M. Piezoelectrically controlled scanning Fabry–Perot spectrometer for emission line studies of extended astronomical objects. Opt. Eng. 27 (12), 121088, 1988.

Che, C., Evans, R.J., Tucker, R.J. Signal processing for optical power spectrum monitoring. Proc. ACSSC, 559–563, 2006.

Conde, M., Smith, R.W. Spatial structure in the thermospheric horizontal wind above Poker Flat, Alaska, during solar minimum. J. Geophys. Res. 103, 9449, 1998.

Dahlgren, H., Ivchenko, N., Sullivan, J., Lanchester, B.S., Marklund, G., Whiter, D. Morphology and dynamics of aurora at fine scale: first results from the ASK instrument. Ann. Geophys. 26, 1041–1048, http://dx.doi.org/10.5194/angeo-26-1041-2008, 2008a.

Dahlgren, H., Ivchenko, N., Lanchester, B.S., Sullivan, J., Whiter, D., Marklund, G., Stromme, A. Using spectral characteristics to interpret auroral imaging in the 731.9 nm O^+ line. Ann. Geophys. 26, 1905–1917, http://dx.doi.org/10.5194/angeo-26-1905-2008, 2008b.

Daly, J.T., Bodkin, W.A., Schneller, W.J., Kerr, R.B., Noto, J., Haren, R., Eismann, M.T., Karch, B.K. Tunable narrow-band filter for LWIR hyperspectral imaging. Proc. SPIE 3948, 104–115, 2000.

De Gennes, P.G., Prost, J. The Physics of Liquid Crystals. Oxford University Press, Oxford, 1993.

Gerrard, A.J., Meriwether, J.W. Initial daytime and nighttime SOFDI observations of thermospheric winds from Fabry–Perot Doppler shift measurements of the 630-nm OI line-shape profile. Ann. Geophys. 29, 1529–1536, http://dx.doi.org/10.5194/angeo-29-1529-2011, 2011.

Gustavsson, B. Three dimensional imaging of aurora and airglow. Doctoral Thesis, IRF Scientific, Report 267, September 2000.

Hernandez, G., Mills, O.A. Feedback stabilized Fabry–Perot interferometer. Appl. Opt. 12, 126–130, 1973.

Jia, D.Y., Ding, T.H. Detection of foreign materials in cotton using a multi-wavelength imaging method. Meas. Sci. Technol. 16 (6), 1355–1362, 2005.

Jokiaho, O., Lanchester, B.S., Ivchenko, N., et al. Rotational temperature of N_2^+ (0, 2) ions from spectrographic measurements used to infer the energy of precipitation in different auroral forms and compared with radar measurements. Ann. Geophys. 26, 853–866, 2008.

Jones, D.H., Shopbell, P.L., Bland-Hawthorn, J. Detection and measurement from narrow-band tunable filter scans. MNRAS 329, 759, 2002.

Lanchester, B.S., Ashrafi, M., Ivchenko, N. Simultaneous imaging of aurora on small scale in OI (777.4 nm) and N21P to estimate energy and flux of precipitation. Ann. Geophys. 27, 2881, 2009.

Laux, C.O. Radiation and Nonequilibrium Collisional-Radiative Models. Available at: http://www.specair-radiation.net, 2002.

Nelder, J.A., Mead, R. A simplex method for function minimization. Comput. J. 7 (4), 308–313, 1965.

Pallamraju, D., Baumgardner, J., Chakrabarti, S. HIRISE, a ground based High Resolution Imaging Spectrograph using Echelle grating for measuring daytime airglow/auroral emissions. J. Atmos. Sol. Terr. Phys., 2001.

Patel, J.S., Wullert, J.R.I. Frequency locking of a tunable liquid-crystal filter. J. Appl. Phys. 71 (5), 2464–2466, 1992.

Pifferi, A. et al. Four-wavelength time resolved optical mammography in the 680–980 nm range. Opt. Lett. 28 (13), 2003.

Prasad, K.M., Bapat, R.B. The generalized moore-penrose inverse. Linear Algebra Appl. 165, 59–69, 1992.

Rees, D., McWhirter, I., Hays, P.B., Dines, T. A stable, rugged, capacitance-stabilised piezoelectric scanned Fabry–Perot etalon. J. Phys. E Sci. Instrum. 14, 1320, 1981.

Romick, G.J., Degen, V., Stringer, W.J. The altitude profile of the N_2^+ first negative rotational temperature in an auroral arc. J. Geophys. Res. 83, 1978.

Schneller, W.J., Noto, J., Kerr, R.B., Doe, R.A. Liquid crystal Fabry–Perot etalons, in: Proc. SPIE 3355, Optical Astronomical Instrumentation, vol. 877, 1998.

Semeter, J., Lummerzheim, D., Haerendel, G. Simultaneous multispectral imaging of the discrete aurora. J. Atmos. Sol. Terr. Phys. 63, 1981–1992, 2001.

Shiokawa, K. et al. New auroral spectrometer using an acousto-optic tunable filter. Adv. Polar Upper Atmos. Res. 16, 146–156, 2002.

Sigernes, F. et al. Multipurpose spectral imager. Appl. Opt. 39 (18), 2000.

Sigernes, F. et al. Hyperspectral all-sky imaging of auroras. Opt. Express 29 (25), 27650–27660, 2012.

Sivjee, G., Hallinan, T., Swenson, G. Fabry–Perot-interferometer imaging system for thermospheric temperature and wind measurements. Appl. Opt. 19, 2206–2209, 1980.

Steen, Å., An auroral large imaging system in northern scandinavia, in: Proc. 9th Symposium on European rocket and balloon programmes and related research, Lahnstein, FRG, pp. 299–303, European Space Agency, ESA SP-291, 1989.

Syrjäsuo, M.T., Pulkkinen, T.I., Janhunen, P., Viljanen, A., Pellinen, R.J., Kauristie, K., Opgenoorth, H.J., Wallman, S., Eglitis, P., Karlsson, P., Amm, O., Nielsen, E., Thomas, C. Observations of substorm electrodynamics using the MIRACLE network, in: Kokubun, S., Kamide, Y. (Eds.), Substorms-4. Terra Scientific Publishing Company, Tokyo, pp. 111–114, 1998.

Vaughan, J.M. The Fabry Perot Interferometer. Taylor and Francis Group, Great Britain, 1989.

Zhang, H., Wavelength tunable devices based on holographic polymer dispersed liquid crystals, PhD Thesis, Kent State University, 2008.